![Universiteit Leiden - The Netherlands logo]

Assembling anisotropic colloidal building blocks

Meester, V.

Citation

Meester, V. (2018, June 7). *Assembling anisotropic colloidal building blocks*. *Casimir PhD Series*. Retrieved from https://hdl.handle.net/1887/62808

Cover Page

Universiteit Leiden

Author: Meester, V.
Title: Assembling anisotropic colloidal building blocks
Issue Date: 2018-06-07

ANISOTROPIC DISTORTIONS IN HEXAGONAL CRYSTALS AT FLUID INTERFACES

Abstract

Defects in colloidal crystals can be induced by a vacancy, interstitial, or by impurities and influence crystal properties such as the mechanical strength and orientation of the crystal. We here investigated how elongated particles distort the hexagonal order in a crystal of repulsive pMMA spheres at a fluid interface. The impurities are dumbbells constructed from two pMMA spheres, with different distances between the two spheres s_{DB}. Our study revealed that the number of nearest neighbors increased with s_{DB} from six to eight spheres. We analyzed both the orientation of the dumbbell with respect to the crystal orientation and the position of the surrounding spheres with respect to the dumbbell orientation. The preferred orientation of the dumbbell depended on the lattice spacing and s_{DB}. In crystals with large lattice spacings no preferred orientation was observed. At short lattice spacings dumbbells with seven and eight nearest neighbors preferentially aligned parallel to the crystal orientation whereas at six nearest neighbors a preferential orientation of 30° with the crystal orientation was measured. The repulsive interaction of the dumbbell with the surrounding spheres restricted the rotational motion of the dumbbell. Positional information of the surrounding spheres showed that all dumbbells anisotropically distorted the hexagonal order in the crystal and that the position of the neighboring spheres depended on the orientation of the dumbbell. Dumbbells with $s_{DB} = 1.03 \pm 0.19\ d$, where d is the diameter of the spheres, occupied one lattice site in the hexagonal crystal and distorted the positional order of the neighboring spheres only locally. Dumbbells with $s_{DB} = 1.27 \pm 0.14\ d$ were surrounded by seven nearest neighbors and distorted the translational order in the crystal by the insertion of two semi-infinite rows in the crystal. Dumbbells with $s_{DB} = 1.42 \pm 0.17\ d$ and eight nearest neighbors occupied two lattice sites and the hexagonal crystal was distorted only locally.

6.1 Introduction

The presence of defects is inevitable in colloidal crystals. Defects distort the structural order of colloids either locally by point defects such as vacancies or interstitials resulting in disclinations and dislocations, or by larger defects such as grain boundaries.[158] These imperfections can influence the mechanical strength of the crystal[159], change the crystal growth direction[160], enhance or deteriorate photonic properties[161,162] and induce melting[163]. The origin of a defect can either be a particle not positioned at a lattice site resulting in a point defect[164], curvature of the substrate inducing topological defects[37,165–168], or the interference of impurities or dopants[34].

Spherical impurities are observed to frustrate the crystal, inhibit crystal growth[34] and influence the segregation of grain boundaries[169]. By doping a crystal of spheres with dumbbells, consisting of two connected spheres, the dumbbells formed dislocation cages which influenced the dislocation dynamics.[38,39] Whereas in crystals of spheres the dislocation motion is unrestricted, the steric restriction of two connected spheres resulted in glassy dynamics. Anisotropic impurities could therefore be promising dopants to tune mechanical or physical properties of the crystal such as the crystallization dynamics and mechanical strength. Additionally, the influence of anisotropic impurities on crystals is relevant for understanding virus-capsid formation where anisotropically shaped defects are observed in immature virus particles.[170]

We studied how hexagonal crystals of highly repulsive spheres were distorted by dumbbell impurities of different dimensions. We formed colloidal crystals on a flat interface between an aqueous and an organic phase, to investigate both the structural order in the crystal as well as the dynamic behavior of the dumbbells with confocal microscopy. The dumbbells distorted the hexagonal order of the surrounding spheres anisotropically and the nature of the defects induced by the impurities depended on the distance between the two spheres forming the dumbbell, the orientation of the dumbbell and the degree of confinement at the interface. We also show that the anisotropic landscape around the dumbbell leads to a preferred dumbbell orientation at short lattice spacings.

6.2 Experimental Methods

Materials

Methacrylic acid (MA, 99.8% extra pure, stabilized), Cyclohexyl bromide (CHB, 99%, purified by filtering through activated alumina adsorbents), Glycerol (99+%), N,N-Dimethylethanolamine (99%) and dodecane (mixture of isomers) were purchased from Acros Organics. The cis-decahycronaphtalene (cis-decalin, 99%), octyl mercaptan($\geq$98.5%), ethanol (96%), ethylene glycol dimethacrylate (EGDM, 98%), methyl methacrylate (MM, 99%, contains $\leq$30 ppm MEHA as inhibitor), 2,2'-Azobis(2-methyl-propionitrile) (AIBN, $\geq$98%), N,N-Dimethylformamide ($\geq$99.8%) and rhodamine B isothiocyanate (RITC, mixed isomers) were purchased from Sigma-Aldrich. Exxson mobil chemical kindly provided Exxsol D120 ($\geq$98%) and 4-aminostyrene was purchased from Alfa Aesar. For stabilization of the pMMA spheres a poly(12-hydrostearic acid) graft polymer (PHS-g-pMMA, 45% solution in a 2:1 (w/w) ethyl acetate/butyl acetate mixture) was synthesized.[171,172] The water used was deionized using a Millipore Filtration System (MilliQ Gradient A10), resulting in a resistivity of 18.2 M$\Omega\cdot$cm.

Methods

Synthesis of core-shell pMMA spheres   pMMA spheres of 2.00 ± 0.05 μm in diameter with a fluorescent core, a non-fluorescent shell (10 nm) and a crosslink density of 2% wt were synthesized according to a dispersion polymerization method developed R.P.A. Dullens *et al.*[171] and adjusted by M.T. Elesser *et al.*[172,173].

Preparation rhodamine aminostyrene   To image the pMMA colloids with confocal microscopy rhodamine aminostyrene (RAS) was bound covalently to the pMMA particles during synthesis. This dye was prepared by dissolving 73.25 mg RITC in 9.77 g DMF, followed by the addition of 75 μL 4-aminostyrene. After 10 minutes of stirring the mixture was transferred to a 50 mL round bottom flask and connected to a rotation evaporator (Buchi rotavapor R-210). The reaction flask was placed in a preheated 40°C waterbath and stirred at 30 rpm at a 45° angle. The solvent was gradually removed from the reaction mixture by maintaining the pressure at 0.06 mbar for 3.5 days using an Edwards RV3 vacuum pump. The purple solid product (RAS) was stored at -20°C.

Preparation monomer solution   To a 9.5 g solution of MM:MA (49:1) 0.0102 g of RAS dissolved in 0.310 g acetone was added. This mixture was placed in the ultrasonic bath for several minutes and vortexed for 1h. Subsequently, the mixture was filtrated using a 0.45 μm PTFE Whatman filter to remove undissolved dye, yielding the filtrated monomer solution.

Synthesis fluorescent pMMA cores   The synthesis was performed in a round bottom reaction flask which was placed in a preheated oil bath (83°C), connected to a 16°C cooler and brought under a nitrogen atmosphere. To the reaction flask a mixture of 10.32 g of hexane:ExxsolD120 (2:1), the filtrated monomer solution, 0.103 g AIBN, 71.4 μL octyl mercaptan and 1.03 g PHS-g-pMMA was added under magnetic stirring at 280 rpm. After six minutes a blue glow appeared in the reaction mixture, indicating pMMA nuclei had formed. Immediately after this observation a crosslink solution containing 3.32 g hexane:ExxsolD120 (2:1) and 190 μL of EGDM was added gradually to the reaction mixture; 10 min at 20 μL/min followed by 28 min at 56 μL/min. After addition of the crosslink solution the reaction mixture was stirred for another 2h in the oil bath. The obtained pMMA cores were washed and transferred to dodecane.
Covalent binding of the PHS-g-pMMA stabilizer molecules to the colloids was achieved by a locking procedure. This procedure was also performed after the shell formation. Covalent binding was achieved by transferring the pMMA colloids in dodecane to a round bottom flask which was placed in a preheated oil bath (130°C), connected to a 16°C cooler and kept at a constant nitrogen atmosphere. The dispersion was magnetically stirred at 280 rpm and when the temperature of the dispersion reached 120°C DMAE (0.2 wt% with respect to the dispersion) was added. The reaction mixture was stirred for another 2h. The resulting pMMA cores were 1.80 ± 0.06 μm in diameter (see Figure 6.1A).

Shell growth   A non-fluorescent shell was grown around the fluorescent pMMA cores to improve particle tracking in confocal microscopy images. The reaction was performed in a round bottom flask placed in a preheated oil bath (83°C), connected to a 16°C cooler while kept under nitrogen atmosphere. To this flask 8.42 g of pMMA cores in hexane:ExxsolD120 (1:1), 0.03368 g AIBN (2%wt with respect to monomer) and 0.113 g octyl mercaptan (4%wt with respect to momomer) were added while magnetically stirring at 300 rpm. After a few minutes of stirring a mixture containing 3.11 g hexane:ExxsolD120 (1:1), 2.83 g MM:MA (49:1), 0.0707 g EGDM, 0.02836 g AIBN (0.4%wt with respect to total syringe volume), 0.014 g octyl mercaptan and 0.014 g PHS-g-pMMA was slowly added over the course of 30 min at 273 μL/min. After addition the reaction was stirred for another hour in the oil bath before cooling down. The procedure to covalently bind the stabilizer molecules to the particles was repeated and the obtained core-shell particles were 2.00 ± 0.05 μm in diameter (Figure 6.1B and 6.1C).

Setup for a flat fluid interface   A flat interface between two liquids was formed using a specially designed interface setup (Figure 6.2). The details of this setup are based on the design of the interface cell of Aveyard *et al.*[174] and have been further developed by D. ten Napel *et al.*[175]. Here, a aluminum-Teflon ring was inserted into a glass holder, the outer ring. Since aqueous solvents have a high
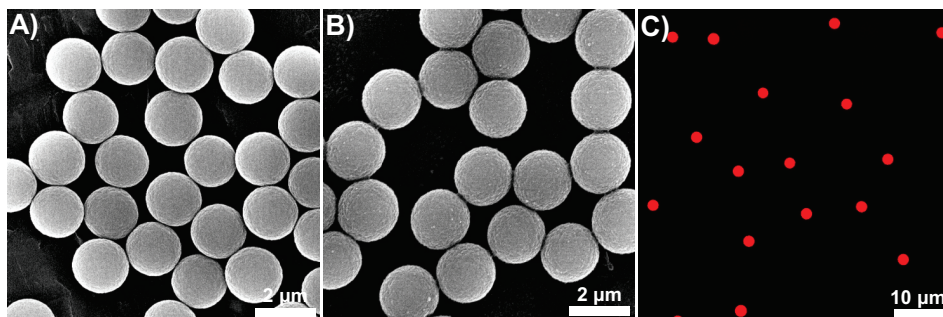
FIGURE 6.1: SEM micrographs of A) fluorescent pMMA cores of 1.80 ± 0.06 μm in diameter and B) pMMA core-shell particles of 2.00 ± 0.05 μm in diameter. C) Confocal microscopy image of the pMMA core-shell particles.

affinity for aluminum and organic solvents for Teflon, the interface between the two solvents aligned with the Teflon-aluminum transition in the ring. By adjusting the volumes of the two liquids a flat interface could be created at this transition. In our setup the outside of the ring consisted of aluminum, whereas the inside had an aluminum and a Teflon part. Small aluminum legs allowed the adjustment of the height of the aqueous liquid inside the ring. The aluminum-Teflon interface inside the ring was positioned at 1 mm from the bottom of the glass coverslip. To image the interface with confocal microscopy an 60x magnification objective (NA = 0.70), with a working distance of 2.6 - 1.8 mm was used. An illustration of the interface cell and a cross section of the setup are shown in Figure 6.2A and B, respectively.

To form a flat fluid interface 1 mL of glycerol:water (85:15 w/w) was added to the glass holder, followed by the placement of the aluminum-Teflon ring. Another 0.3-0.4 mL of glycerol:water (85:15 w/w) was added until the aluminum part on the inside of the ring was completely wetted. On top of the aqueous layer 0.3-0.4 mL of CHB:cis-decalin (70:30 w/w) was deposited forming a flat interface between the two liquid phases. Finally, 40 μL of a 0.08-0.20 wt% pMMA colloid dispersion in CHB:cis-decalin (70:30 w/w) was gently added on top of the organic layer. The setup was covered with a glass cover which was sealed with grease (Apiezon grease M) to close the system and avoid evaporation. The sample was imaged one to three days after preparation to allow the interface to saturate with particles.

Imaging and analysis The synthesized pMMA particles were imaged using a FEI nanoSEM scanning electron microscope (SEM) at 80 kV. The diameter of the pMMA cores and core-shell particles was determined by measuring the circumference of >100 particles in SEM micrographs with ImageJ.
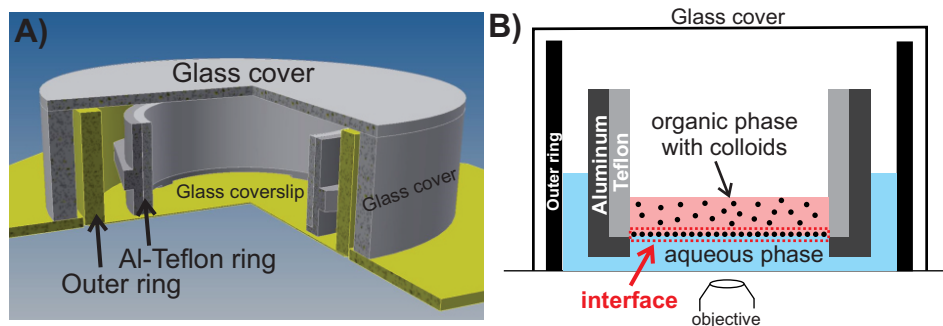
FIGURE 6.2: A) Illustration of the interface cell used to form a flat interface between an aqueous and an organic liquid. B) Cross section of the interface setup. The aqueous liquid has affinity for the aluminum part of the ring, while the organic liquid has affinity for the Teflon part. The interface will therefore be pinned at the transition between these two materials on the inside of the ring forming a flat interface. The interface is positioned at 1 mm from the bottom of the coverslip and the system is closed by a glass cover to avoid evaporation of the solvents.

The ordering of pMMA colloids at the flat interfaces was studied using a Nikon Eclipse Ti microscope. The microscope was equipped with an A1R confocal scan head and a CFI S Plan Fluor ELWD 60x C with a working distance of 2.6 - 1.8 mm and NA = 0.70. The RAS dyed cores of the pMMA spheres were excited with a laser wavelength of 561 nm and detected at 625 nm.

The coordinates and centers of mass of the particles in confocal images were determined using a Python implementation of the Crocker and Grier algorithm, TrackPy.[176,177] The anisotropic impurities were analyzed using a different implementation of this algoritm that accounts for the bias due to overlapping particle signals.[178] The crystal orientation α was measured manually by connecting the centers of mass of at least ten spheres along a crystal axis.

6.3 Results and Discussion

6.3.1 Ordering of repulsive spheres at a flat fluid interface

To determine the effect of anisotropic particles on a crystal of repulsive spheres at a fluid interface, we first analyzed the ordering of merely spheres. To exclude curvature effects on the motion and positioning of the particles in the crystal a special interface cell was used to yield a flat interface between CHB:cis-decalin (70:30 w/w) and glycerol:water (85:15 w/w) (see Figure 6.2). pMMA spheres of 2.00 ± 0.05 μm in diameter were dispersed in the organic liquid which was deposited on top of the aqueous phase. After an equilibration time of one to three
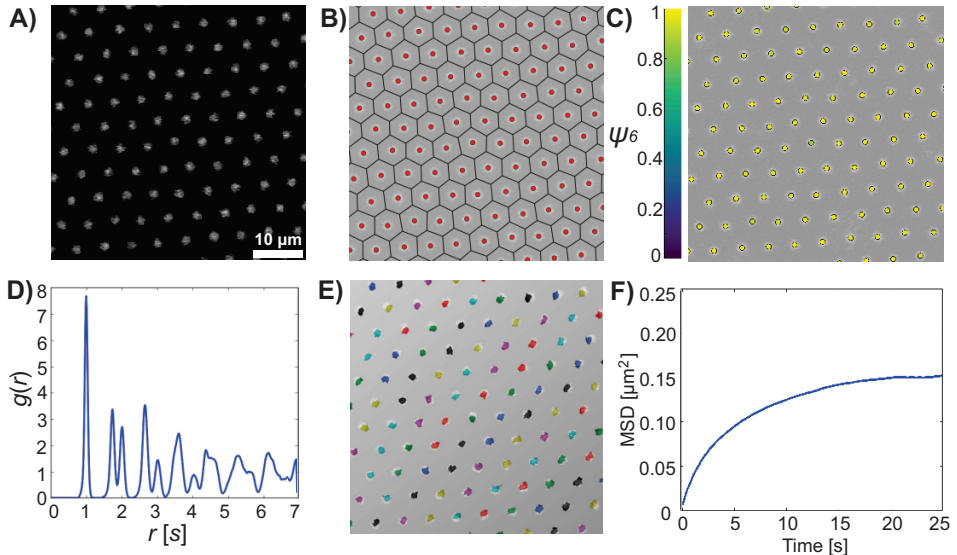
FIGURE 6.3: Ordering of repulsive pMMA spheres at a flat fluid interface. A) Confocal microscopy image of pMMA spheres of 2.00 ± 0.05 μm in diameter d bound to the interface between an CHB:cis-decalin (70:30 w/w) and a glycerol:water (85:15 w/w) phase. B) Voronoi diagram showing that all particles in (A) have six nearest neighbors and no disclinations are formed. C) The hexagonal bond order parameter, $|\psi_6|$, has values close to 1 for all particles, indicating that the spheres are ordered on an hexagonal lattice. D) The radial distribution function ($g(r)$) of the spheres collected from 1800 measurements in one minute. The peaks at large radial distances indicate that the hexagonal order ranges to distances of 7s, where s is the average lattice spacing in the crystal, $s = 2.73d$. The peak at 1s originates from the six NNs of the spheres. E) The trajectories that the colloids in (A) travelled in one minute (1800 measurements). The motion of the spheres is confined to a single lattice site in the crystal. F) The mean square displacement (MSD) of the spheres levels off at 20 s at 0.15 μm^2 confirming that the translational motion of the particles is restricted.

days spheres were observed both at the interface as well as in the upper organic phase. The non-adsorbed particles diffused in three dimensions, while the interfacially bound pMMA spheres moved in the two dimensions of the interfacial plane only. Interparticle distances of several times the diameter of the spheres were observed, induced by the strong Coulomb repulsions between the charged particles. The average interparticle distance between the spheres in bulk was at least two times larger compared to the interfacially bound spheres. This effect has been attributed to the presence of mirror charges originating from ions in the aqueous phase that screen the charge of the interfacially bound pMMA spheres, resulting in an additional Coulomb attraction[30,179,180].

The interfacially bound pMMA spheres positioned in a regular hexagonal pattern (see Figure 6.3A). The Voronoi diagram of this pattern shows that all particles are surrounded by six nearest neighbors (NNs), see Figure 6.3B. The local structural ordering of the crystal was analyzed by calculating the hexagonal bond order parameter ψ_6, which is defined as:

$$\psi_{6,j} = \frac{1}{N} \sum_{k=1}^{N} e^{6i\theta_{jk}}, \tag{6.1}$$

where N refers to the number of nearest neighbors of particle j and θ_{jk} is the angle between a fixed reference axis and the vector between particle j and neighbor particle k. The absolute value of ψ_6 is an indication of the local hexagonal crystallinity and ranges from 0 to 1, with $|\psi_6|=1$ for perfect hexagonal symmetry. The spheres at the fluid interface have $|\psi_6|$-values close to 1 indicating that the spheres arrange on a hexagonal lattice, see Figure 6.3C.
Positional information was obtained from the radial distibution function, which is defined as:

$$g(r) = \rho \cdot 2\pi r dr \tag{6.2}$$

where ρ is the average particle density in a $2\pi r$ shell with shell thickness dr at a distance r from the center of mass (COM) of the particles. The $g(r)$ shown in Figure 6.3D is constructed from the particle positions extracted from 1800 measurements collected over one minute. Peaks in $g(r)$ are observed up to a distance r of at least seven times the average interparticle distance s between the spheres. Although the spheres are free to diffuse at the interface, the trajectories of the spheres (Figure 6.3E) display that this translational motion is restricted to a lattice site. This is confirmed by the mean square displacement (MSD) of the spheres over time, Figure 6.3F, where the MSD levels off around 20 s at 0.15 μm^2. The degree of confinement is determined by the range of the repulsive and attractive Coulomb forces and depends on the colloid density at the interface.[174,181]

6.3.2   Impurities at a flat fluid interface

Besides individual spheres, impurities were also found at the fluid interface. We classified these impurities into three different classes. The first class includes spherical objects with sizes significantly smaller (Figure 6.4A) or larger (Figure 6.4B) than the diameter, d, of the particles. These objects are side products formed during the synthesis of the pMMA spheres. The effect of the large spherical impurities on the crystal growth of colloidal spheres was studied by Villeneuve *et al.* who found that impurities induce the formation of grain boundaries and inhibit crystal growth.[34] The second type of impurities are circular patterns of spheres with short interparticle distances (Figure 6.4C). These spherical shells are cross-sections of likely aqueous droplets stabilized by colloids in the organic phase
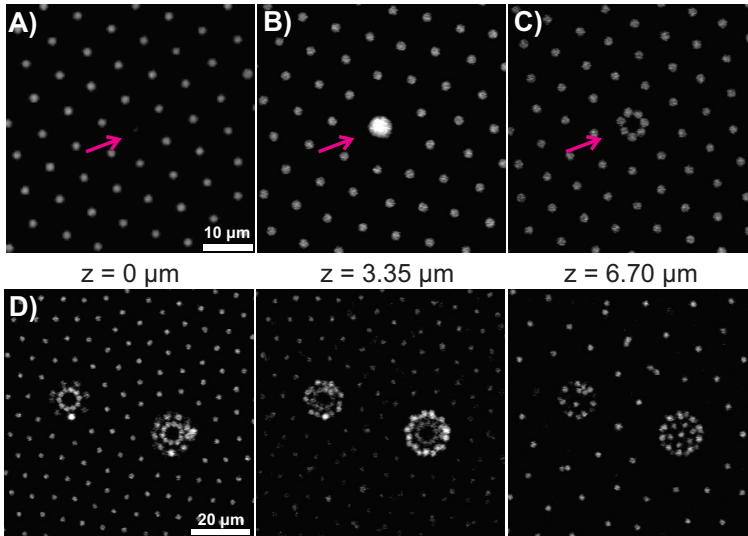
FIGURE 6.4: Confocal microscopy images of spherical and circular impurities observed at an organic-aqueous fluid interface. Spherical particles with a diameter significantly smaller (A) or larger (B) than the average diameter of the spheres. C) Circular structures of particles with short interparticle distances. These patterns are cross-sections of droplets stabilized by pMMA spheres in the organic phase as shown in (D), where z corresponds to the height of the plane in the third dimension with z=0 μm at the interface.
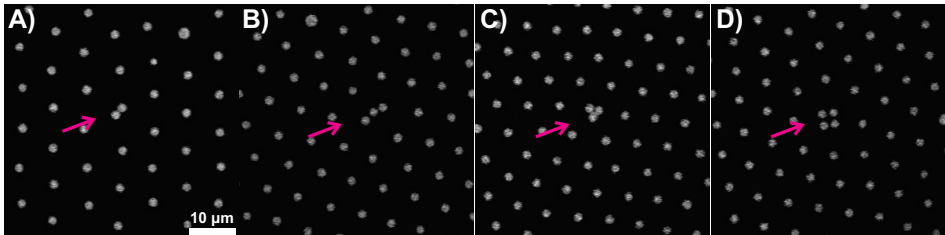

FIGURE 6.5: Confocal microscopy images of anisotropic impurities observed in the two-dimensional crystal of hexagonally ordered repulsive pMMA spheres at the fluid interface. C-F) Anisotropic defects assembled by several spheres such as; chain-like structures(C), dumbbells(D), triangles(E) and squares(F).

(Figure 6.4D). The number of these defects increased with time and temperature, probably due to evaporation and condensation within the interface cell.

In this study we are mostly interested in the third class of impurities; anisotropic mesostructures formed by the assembly of individual spheres with interparticle distances « s. Dumbbell shapes were formed by two spheres (Figure 6.5A), but

different shapes were observed for clusters constructed by three or more particles. For clusters of three particles chain-like structures (Figure 6.5B) were found as well as well-defined triangles (Figure 6.5C). Also for larger clusters compact, such as the square for four spheres (Figure 6.5D), as well as elongated shapes were observed. Similar anisotropically shaped clusters were observed of polystyrene spheres at water-air interfaces[182,183] and of pMMA spheres in bulk after centrifugation[184] and at aqueous-organic interfaces[185].

The interaction of pMMA spheres at an aqueous-organic interface was described by Leunissen *et al.*[28] and Kelleher *et al.*.[179,181] They showed that the net interaction between pMMA spheres bound to an aqueous-organic interface is the sum of Coulomb repulsions originating from the spheres' surface charge and Coulomb attractions due to interaction of the particles with the mirror charges of the neighboring spheres.[28,179,181] Since high wetting angles of the pMMA colloids with the aqueous phase were measured, the system could be described by spheres with charge q arranged on a conducting medium, which is the aqueous phase. This results in a dipolar force between pairs of interfacially bound spheres with pairwise additive interactions. The net interaction of two such particles can therefore be approximated by a pair potential of the form[181],

$$U(r) \simeq \frac{A}{r^3},$$

(6.3)

where $A = p^2/8\pi\epsilon$, with ϵ the dielectric constant of the oil and $p = qd$ the magnitude of the electric dipole moment of the particles and r the interparticle distance. Interestingly, this interaction profile does not allow the formation of the observed mesostructures with much shorter interparticle distances. Other phenomena or additional interfacial forces have to play a role. In the next section we analyse interfacially bound dumbbells and use these findings to speculate on the origin of the anisotropic impurities.

6.3.3   Interfacially bound dumbbells

To study the effect of the anisotropy of impurities on the hexagonal order of spheres, we analyzed the distortion induced by elongated dumbbell shapes. The interfacially bound dumbbells were characterized by their position at the interface and their dimensions. Over 95% of the dumbbells aligned with their long axis parallel to the interfacial plane. We expected preferential wetting of the particles by the organic liquid, since Kelleher *et al.* measured contact angles close to 180° for pMMA spheres at an interface between aqueous 70 wt% glycerol solution (10 mM NaCl) and an organic phase consisting of CHB, hexane, and dodecane (5:3:2 v/v). Nevertheless, we observed that the motion of the anisotropic particles was restricted to the two dimensions of the interfacial plane, confirming
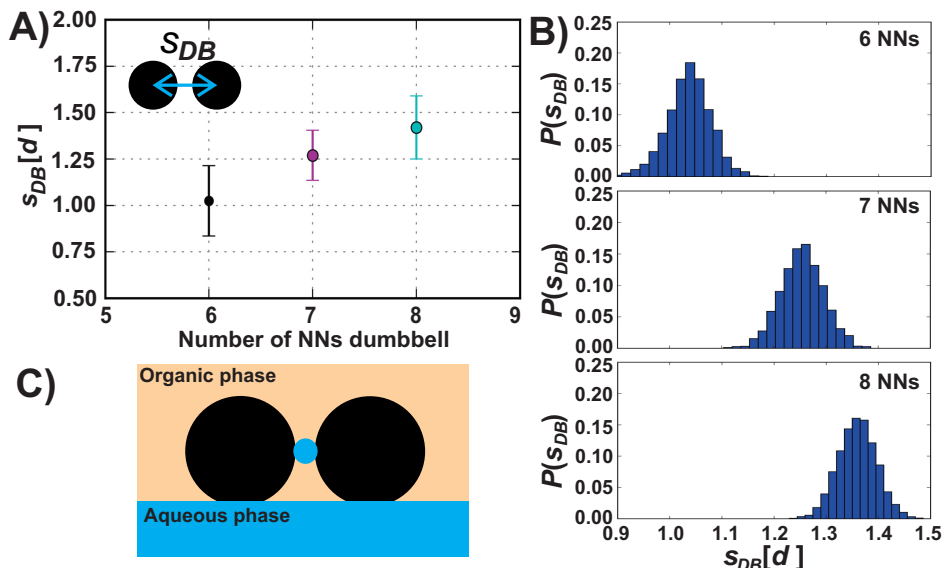
FIGURE 6.6: The intradumbbell distance (s_{DB}) and the number of nearest neighbors (NNs) of interfacially bound dumbbells. The diameter of the spheres, $d = 2.00 \pm 0.05$ μm. A) s_{DB} of dumbbells with six, seven or eight NNs. The number of NNs increases with the distance between the two spheres of the dumbbell. s_{DB} was determined for >225 different dumbbells. B) s_{DB} of individual dumbbells with six, seven or eight NNs, calculated from > 3100 measurements collected over several minutes. The pixelsize is 0.07-0.10d. Since the standard deviations measured in s_{DB} are close to the pixelsize, s_{DB} is essentially constant for individual dumbbells. C) Illustration of a dumbbell at an organic-aqueous interface formed by a small aqueous droplet connecting two spheres.

that the colloids were interfacially bound. In our analysis, dumbbells with their long axis aligned parallel to interfacial plane were examined only.

We found that the distance between the two spheres forming the dumbbell, which we from here on refer to as the intradumbbell distance s_{DB}, differed per particle. Furthermore, dumbbells with six, seven or eight NNs were observed. Analysis of s_{DB} and the number of NNs of >225 dumbbells revealed a relation between the two, where the number of NNs increased with increasing s_{DB} (Figure 6.6A). Figure 6.6B shows s_{DB} of individual dumbbells with six, seven or eight NNs from at least 3100 measurements collected in several minutes. s_{DB} deviates at max 0.1d from the average s_{DB} value, which is similar to the pixelsize and likely caused by a tracking error. We therefore assume that s_{DB} is fixed for each dumbbell.

These findings allow us to speculate on the origin of the formation of dumbbells and larger structures at an organic-aqueous interface. It was suggested that residual van der Waals forces between the spheres could cause attraction.[185] If van der
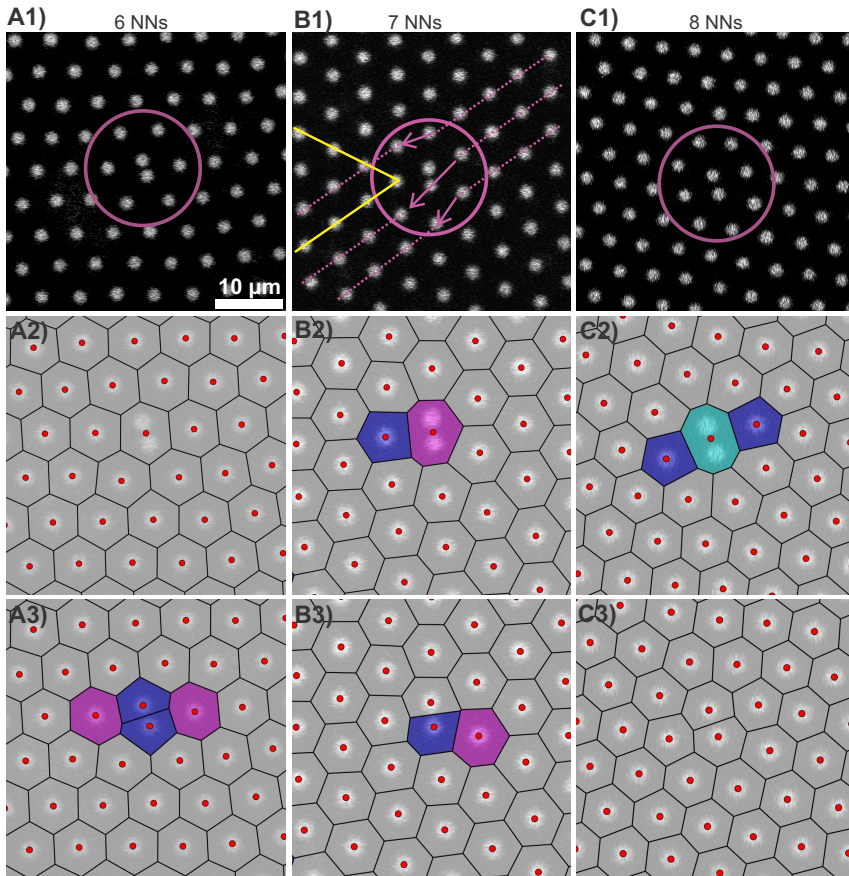
FIGURE 6.7: Dislocations induced by dumbbells with six, seven and eight NNs. Confocal microscopy images of dumbbells with six (A1), seven (B1) and eight (C1) NNs. In B1) the line dislocation is visualized with by the yellow lines. Corresponding Voronoi diagrams of the microscopy images in A1-C1. The dumbbell is considered as one particle in A2-C2 and as two individual spheres in A3-C3. The Voronoi cells are colored according to the coordination number, z_i, of the colloids; purple for $z_i=5$, grey for $z_i=6$, magenta for $z_i=7$ and turquoise for $z_i=8$. A dumbbell with six NNs substitutes one lattice position in the hexagonal crystal without the formation of dislocations (A2 and A3). At seven NNs a five-and-seven disclination pair is formed resulting in the insertion of two semi-infinite rows in the hexagonal crystal (B2 and B3). At eight NNs the dumbbell substitutes two lattice sites in the hexagonal crystal.

Waals forces between the spheres would induce the formation of dumbbells, s_{DB} would approximately be equal to the diameter of the spheres. Since we found
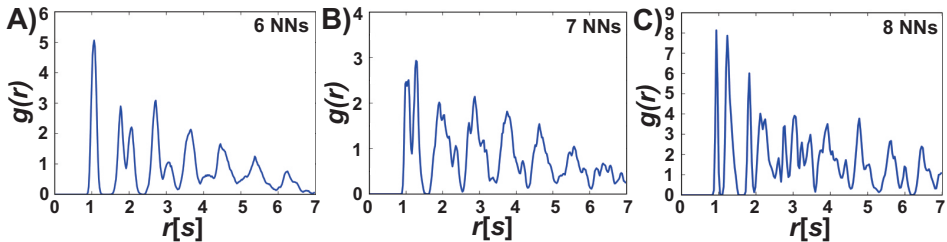
FIGURE 6.8: Radial distribution functions of crystals around typical dumbbells with A) six, B) seven and C) eight neighbors with the COM of the dumbbell at r=0. Constructed from at least 3100 measurements collected over several minutes.

differences in s_{DB} much larger than the polydispersity of the spheres, residual van der Waals forces do not explain the formation of the clusters. Distortions of the interface induced by surface roughness could also induce attraction[186], but it is unlikely that this would result in dumbbells with different s_{DB}. A plausible explanation is the interference of interfacial contaminations[183]. Since we observed larger droplets covered with spheres, it is likely that smaller droplets are also present at the interface. Impurities with sizes close to or smaller than the diffraction limit of optical microscopy, such as droplets or nanobubbles[187–189], could connect spheres to form larger structures, as illustrated in Figure 6.6C. This explanation is also in agreement with the fixed s_{DB} for individual dumbbells, but deviating values for s_{DB} of different dumbbells.

Confocal microscopy images of typical interfacially bound dumbbells with six, seven or eight NNs are shown in Figure 6.7A1, 6.7B1 and 6.7C1, respectively. By performing Voronoi tesselations on these images the disclinations and dislocations induced by the different dumbbells were visualized. We show two Voronoi diagrams: one where the dumbbell is treated as a single particle and one where the dumbbell is viewed as two individual spheres.

When the dumbbell is viewed as one particle, the Voronoi diagram of a typical dumbbell with six NNs shows that all particles have the same coordination number, z_i=6 (Figure 6.7A2). The Voronoi diagram obtained when the dumbbell is taken as two individual spheres reveals a dislocation pair, with z_i=5 at the spheres forming the dumbbell and z_i=7 at two of the NNs (Figure 6.7A3). This indicates that the dumbbell substitutes a single lattice site in the hexagonal crystal without long-range distortions of the orientational and translational order. A five-and-seven coordinated disclination pair is introduced for the dumbbell with seven NNs, see Figure 6.7B2 and B3. The isolated dislocation distorts the translational order in the hexagonal crystal by the insertion of two semi-infinite rows in the crystal, as illustrated by the yellow lines in the corresponding confocal image in Figure 6.7B1. At eight NNs a z_i=8 is located at the dumbbell and two of

the NNs have z_i=5, which is an unusual dislocation (Figure 6.7C2). The Voronoi diagram of the two separate spheres reveals that the dumbbell substitutes two lattice positions in the hexagonal crystal, without long-ranged distortions of the crystal (Figure 6.7C3). We expect that the number of lattice sites in the hexagonal crystal occupied by elongated impurites will increase with the length of the particle. For large s_{DB} dumbbells will act as separate spheres, but linear impurities constructed by more than two spheres, such as chains, could provide this information.

Positional information of the spheres surrounding the dumbbell was obtained from $g(r)$ with the COM of the dumbbell as origin. Peaks in $g(r)$ are observed to a distance r of at least seven times the lattice spacing s for dumbbells with six, seven as well as eight NNs, see Figure 6.8. This indicates that local order is maintained for the spheres around the dumbbells. Interestingly, the shape of the radial distribution function strongly depends on the number of NNs. The radial distribution function of the dumbbell with six NNs (Figure 6.8A) is largely in agreement with $g(r)$ obtained for spheres indicating that overall the hexagonal order of the crystal was conserved (Figure 6.3D). Only small differences are found in the width and position of the peaks. For example, the peak of the NNs, at $r = 1s$ for spheres, is broader and slightly shifted to a larger distance r. At seven NNs the location of the peaks in the $g(r)$ (Figure 6.8B) deviate from $g(r)$ of spheres. Whereas all NNs are positioned at $r = 1s$ for spheres, the seven NNs are observed at different distances r from the dumbbell, resulting in a partly splitted peak around r=1s. At eight NNs the peak at $r = 1s$ has splitted completely into two separate peaks (Figure 6.8C). These findings denote that the distortion of the hexagonal order by dumbbells depends on the length of the dumbbell, s_{DB}. In the next sections we took the anisotropy of the dumbbell in our analysis into account to investigate the dynamics of dumbbells with six, seven and eight NNs and their effect on the surrounding crystal, separately.

6.3.4   Dumbbell orientation and crystal distortion

Analysis approach

To study the effect of dumbbell impurities on a hexagonal crystal, the anisotropy of the dumbbell has to be accounted for. We measured both the orientation of the dumbbell with respect to the crystal orientation and the position of the surrounding spheres with respect to the dumbbell orientation. On a two-dimensional hexagonal lattice different axes of reflection symmetry are present. In Figure 6.9A we illustrated the crystal orientation axes which make angles with $\vec{a}_1$ of 0, $\pi/3$ and $2\pi/3$ (green lines) or $\pi/6$, $\pi/2$ and $5\pi/6$ (dotted purple lines). We defined the dumbbell orientation as the angle β, between the long dumbbell axis and the
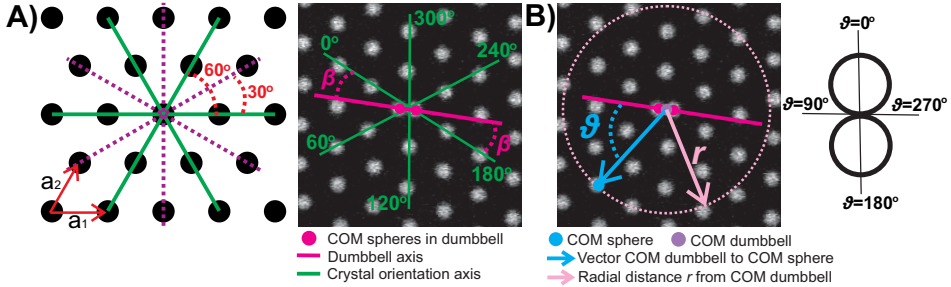
FIGURE 6.9: Illustration of the parameters used to determine the orientation of dumbbells with respect to the crystal orientation and the position of the spheres in the surrounding crystal with respect to the dumbbell. A) Different axes of reflection symmetry are present on a two-dimensional hexagonal lattice. The dumbbell orientation was defined as the angle β between the dumbbell axis and the crystal orientation axes in green. The six-fold symmetry in an hexagonal crystal allowed us to mirror all data of β into the range $\beta \epsilon [0°, 30°]$. Additionally, the average interparticle distance between the spheres in the crystal, s, was also included in the analysis. B) The position of the spheres was described by the distance r between the COM of the sphere and the COM of the dumbbell and the angle ϑ between the dumbbell axis and the vector of the COM of the dumbbell to the COM of the sphere.

crystal orientation axis in green (Figure 6.9A). A preference for a certain value of β would indicate an anisotropic energy landscape. The degree of confinement of the dumbbell also depends on the average lattice spacing s in the hexagonal crystal and the dimensions of the dumbbell and we therefore investigated.

To determine how dumbbells distort the hexagonal order in the crystal, we measured the position of the surrounding spheres with respect to the dumbbell axis. The position of spheres was defined by the radial distance r between the COM of the dumbbell and the COM of the sphere, and the angle ϑ between the vector from the dumbbell to the sphere and the dumbbell axis (Figure 6.9B). Spheres ordered on a perfect hexagonal lattice have equal interparticle distances, and angles of 60° between the vectors with their six NNs. If dumbbell impurities distort the hexagonal order of the surrounding spheres, the neighboring spheres will position at different values of r as a function of ϑ at a given dumbbell orientation β. These parameters are therefore required to determine the distortion of the hexagonal order by dumbbells.

Dumbbell orientation in crystals with different lattice spacings

The orientation of dumbbells in crystals with different lattice spacings s was measured to determine the influence of particle confinement on the motion and position of the dumbbells. Trajectories of dumbbells with six NNs, travelled over
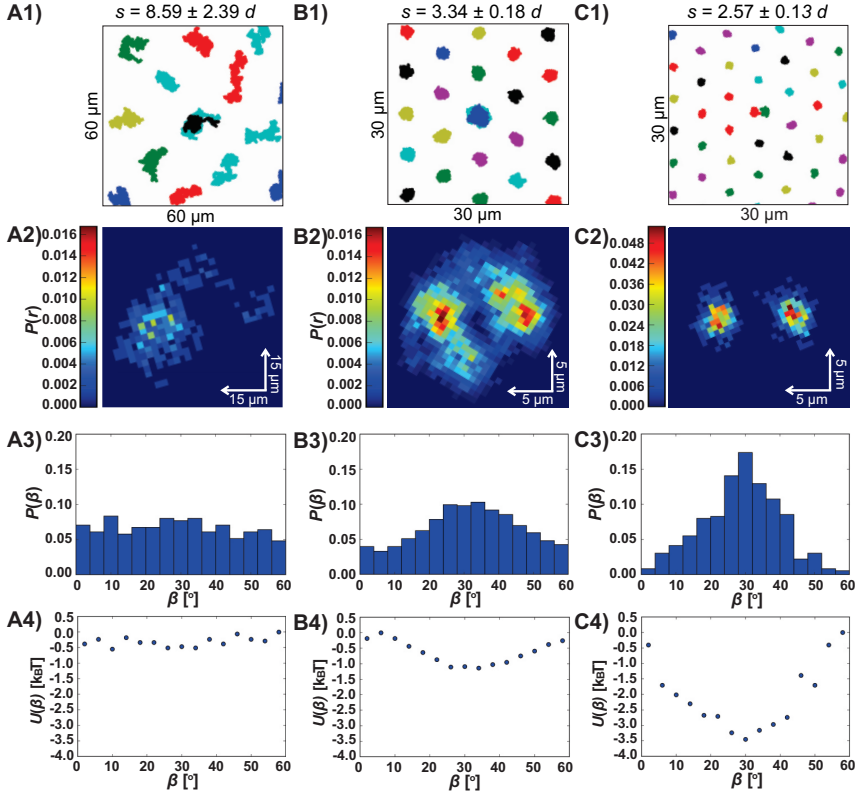
FIGURE 6.10: Trajectories and preferred orientation of individual dumbbells with six NNs in crystals with different s. (A1-A4) $s = 8.59 \pm 2.39d$ (300 measurements in 15 minutes), (B1-B4) $s = 3.34 \pm 0.18d$ (4500 measurements in 15 minutes), and (C1-C4) $s = 2.57 \pm 0.13d$ (360 measurements in 6 minutes). A1-C1) Trajectories of dumbbells and surrounding spheres. At decreasing s the particles are increasingly confined to a lattice position. A2-C2) Probability density plots, $P(r)$, of the position of the dumbbells. At $s = 8.59 \pm 2.39d$ the dumbbell rotated without restrictions and only slight restrictions in the translational motion were observed. At $s = 3.34 \pm 0.18d$, the translational motion of the dumbbell was restricted to one lattice site, but full dumbbell rotation was still allowed. At $s = 2.57 \pm 0.13d$ both the translation and rotation of the dumbbell were resticted. A3-C3) The probability for the dumbbell to orient at a certain value of β, $P(\beta)$, where we combined all data to $\beta \epsilon [0°, 60°]$. A4-C4) The confinement energy $U(\beta)$ corresponding to $P(\beta)$. In a highly fluidic crystal, $s = 8.59 \pm 2.39d$, no preferred dumbbell orientation was observed. At $s = 3.34 \pm 0.18d$ $P(\beta)$ was largest at $\beta = 30°$ corresponding to an confinement energy of -1.1 $k_B T$. Highly confined dumbbells, $s = 2.57 \pm 0.13d$, preferentially oriented at $\beta = 30°$ with an confinement energy of -3.5 $k_B T$.

several minutes in crystals with $s = 8.59 \pm 2.39d$, $s = 3.34 \pm 0.18d$ and $s = 2.57 \pm 0.13d$, are shown in Figure 6.10A1, 6.10B1 and 6.10C1, respectively. The area covered by the dumbbell and the surrounding spheres decreased drastically with decreasing s. The probability density plot of the position of the dumbbell, $P(r)$, in a crystal with $s = 8.59 \pm 2.39d$ shows that the confinement of the dumbbell in the crystal was low with no restrictions in the rotational motion and some restrictions in the translational motion (Figure 6.10A2). At $s = 3.34 \pm 0.18d$ the dumbbell was confined to a lattice position, but full rotation around the COM of the dumbbell was still observed (Figure 6.10B2). At $s = 2.57 \pm 0.13d$ the confinement of the particles increased further leading to large restrictions in both the translational and rotational motion of the dumbbell (Figure 6.10C2).

Due to the anisotropy of the dumbbell we expected that restrictions in the rotational motion would lead to a preference for a certain orientation of the dumbbell with respect to the crystal. We measured the dumbbell orientation, defined by β (Figure 6.9A), for individual dumbbells over time in crystals with different s. At $s = 8.59 \pm 2.39d$ the crystal was highly fluidic and the probability for the dumbbell to orient at a certain value of β, $P(\beta)$, was uniform for all β (Figure 6.10A3). By decreasing s to $3.34 \pm 0.18d$ a non-uniform distribution in $P(\beta)$ was measured with the highest probability at $\beta = 30°$ and the lowest at $\beta = 0°$ and $60°$ (Figure 6.10B3). In crystals with $s = 2.57 \pm 0.13d$ the preference for $\beta = 30°$ became even more significant (Figure 6.10C3).

Using $P(\beta)$ we calculated the confinement potential of the dumbbells, $U(\beta)$, via the Boltzmann distribution:

$$U(\beta) = U_0 - k_B T \ln P(\beta) \qquad (6.4)$$

where k_B is the Boltzmann constant and T the temperature. The energy U is determined with respect to a reference value U_0, which we set at the maximum measured value of U. In Figure 6.10A4-C4 the energy profiles calculated from the probability functions in Figure 6.10A3-C3 are shown, respectively. At large s, $8.59 \pm 2.39d$, the confinement energy was independent of β. In more dense crystals, $s = 3.34 \pm 0.18d$ an energy difference of -1.1 $k_B T$ is observed between $\beta = 30°$ and $\beta = 0°$ or $60°$. The confinement energy increased to -3.5 $k_B T$ when the lattice spacing in the crystal was increased to $s = 2.57 \pm 0.13d$.

Besides analysing individual dumbbells in time we also determined $P(\beta)$ from an ensemble of different dumbbells with six NNs. Analysis of 150 confocal microscopy images of different dumbbells with six NNs in crystals with $s = 3.59 \pm 0.29d$, showed no significant preference for β (Figure 6.11A). In more compact crystals with $s = 2.64 \pm 0.09d$, a preferred orientation of $\beta = 15°-30°$ was observed from analysis of 100 different dumbbells (Figure 6.11B). These results are in agreement with the measurements of individual dumbbells, where a preference for β

= 30° was found as short s.

Our results show that dumbbells with six NNs become more confined to $\beta = 30°$ with decreasing lattice spacing s due to restrictions in the rotational motion. This can be understood by examining the energy landscape around the dumbbell in the hexagonal crystal of spheres. We plotted the energy landscape using the pair potential of individual spheres assuming pairwise additivity, see Equation 6.3. To calculate the pair potential the particle charge q is required. For pMMA spheres of 2.6 μm in diameter dispersed in CHB:hexane:dodecane (5:3:2 v/v) Kelleher *et al.* measured a charge of 530-590e, with e as the elementary charge.[179] Using electrophoresis, Leunissen *et al.* measured a charge of 450e for pMMA colloids of 2.16 μm in diameter in density-matched CHB:cis-decalin.[28] Since our colloids are synthesized according to the same synthetic method[173] and a comparable interface was used, we assumed similar values for q. The dielectric constant of our organic phase, CHB:cis-decalin (70:30 w/w), is 5.6.

We plotted the potential energy, $U(r)$, for a dumbbell particle and six hexagonally ordered spheres. The energy profile around the dumbbell is anisotropic as expected, see Figure 6.12A. Although the energy profile of the individual spheres is isotropic, the potential energy landscape created by the six particles is anisotropic (Figure 6.12B). At equal distance r from the center particle the potential energy is lowest in the direction in between the spheres and highest in the direction of the
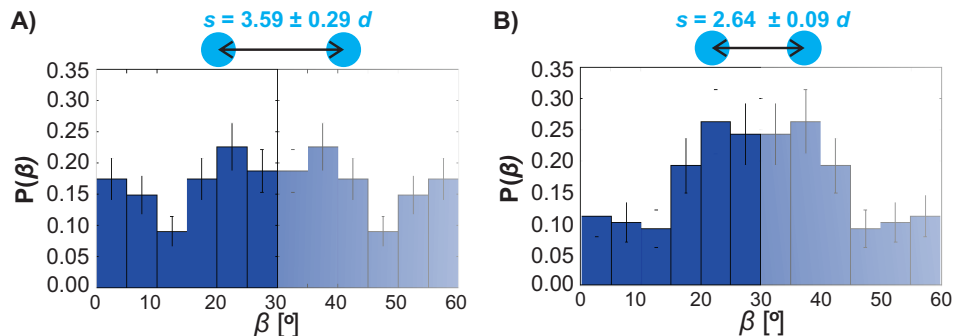

FIGURE 6.11: Dumbbell orientations of an ensemble of dumbbells with six NNs in crystals with different lattice spacing s obtained from confocal microscopy images. β was measured as the angle between the dumbbell axis and the crystal orientation axis closest to the dumbbell axis, therefore $\beta \epsilon [0°, 30°]$. Due to symmetry in the hexagonal crystal we expect the values for $\beta \epsilon [0°, 30°]$ to be symmetric to $\beta \epsilon [60°, 30°]$, respectively. The probability to find a dumbbell with a certain value of β, $P(\beta)$, in crystals with A) s = 3.59 ± 0.29d, where no significant preference in β is observed from analysis of 150 different dumbbells, and at B) s = 2.64 ± 0.09d, where dumbbells preferably oriented at β-values of 15°-30°. 100 different dumbbells were analyzed.
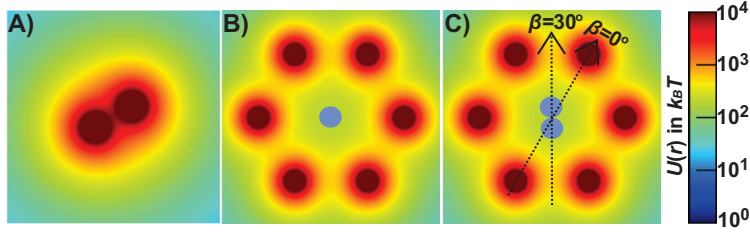
FIGURE 6.12: Potential energy profile around A) a dumbbell and B) six hexagonally ordered spheres. C) Due to the anisotropic energy profile around the dumbbell and inside the hexagon, it is energetically favorable for the dumbbell to orient at $\beta = 30°$.

spheres. Since the dumbbell has an anisotropic interaction itself, the dumbbell experiences the least repulsion at $\beta = 30°$, see Figure 6.12C.

Crystal distortion by dumbbells with six NNs

At short lattice spacings the energy landscape around dumbbells with six NNs is not uniform, which leads to a preferred orientation of the dumbbell. In turn, the anisotropy of the dumbbell would also affect the position of the surroundig spheres in the hexagonal crystal. Although no dislocations were formed by dumbbells with $s_{DB} = 1.03 \pm 0.19d$ and six NNs, small differences were observed in the position and width of the peaks in $g(r)$ for a dumbbell with six NNs in a crystal with $s = 3.34 \pm 0.18d$ (Figure 6.8A), compared to $g(r)$ for hexagonally ordered spheres (Figure 6.3D). This indicates that dumbbells with six NNs in crystals with short lattice spacings change the hexagonal order in the crystal locally. To investigate whether the distance r at which the neighboring spheres were positioned was related to the anisotropy of the dumbbell, we included the angle between the dumbbell axis and the vector of the dumbbell to any neighboring sphere, ϑ, in our analysis (see Figure 6.9B).

We identified and quantified any anisotropic distortion of the crystal by plotting $g(r)$ for restricted angular ranges of ϑ, by defining a restricted angular radial distribution function:

$$g_\vartheta(r) = \rho_\vartheta \cdot \delta\rho r dr, \tag{6.5}$$

where ρ_ϑ is the average particle density in the angular range $[\vartheta \pm \frac{\delta\vartheta}{2}]$ in a $\rho_\vartheta \cdot \delta\rho r dr$ area. We plotted $g_\vartheta(r)$ separately for $\vartheta = 0°$, $15°$, $30°$....$360° \pm \frac{\delta\vartheta}{2}$, with $\delta\vartheta = 15°$, covering the complete radial distribution in 24 intervals of $15°$. In Figure 6.13 four $g_\vartheta(r)$ graphs are shown, containing positional information of spheres surrounding the dumbbell at angles $\vartheta\epsilon[0° , 90°]$, $[90°, 180°]$, $[180°, 270°]$ and $[270°, 360°]$, respectively. The four $g_\vartheta(r)$-plots show peaks at similar distances r, pointing to symmetric behavior of the spheres in the four quadrants around the dumbbell
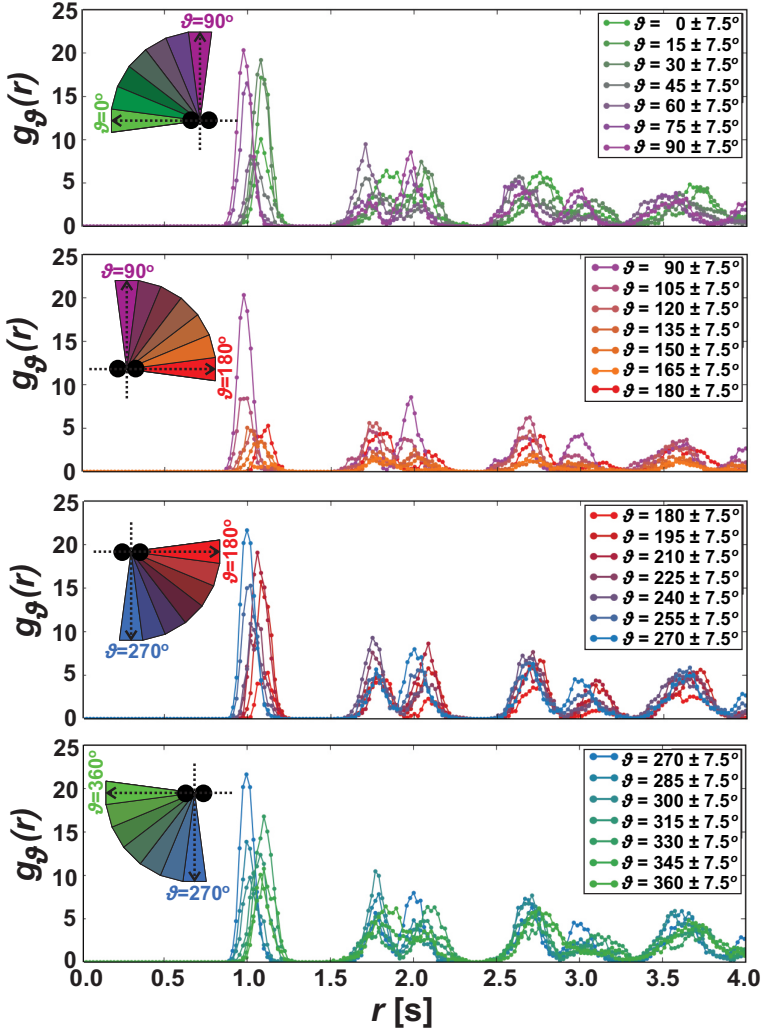
FIGURE 6.13: Restricted angular radial distribution function, $g_\vartheta(r)$, of a dumbbell with six NNs in a crystal with $s = 3.34 \pm 0.18d$, where d is the diameter of the spheres. $g_\vartheta(r)$ was obtained from 4500 measurements collected over 15 minutes with $r = 0$ at the COM of a dumbbell. Four $g_\vartheta(r)$ graphs are shown with positional data of spheres at $\vartheta\epsilon[0°, 90°]$, $[90°, 180°]$, $[180°, 270°]$ and $[270°, 360°]$, respectively. Peaks in the four graphs are observed at similar distances r, pointing to symmetric behavior of the spheres in the four quadrants around the dumbbell.
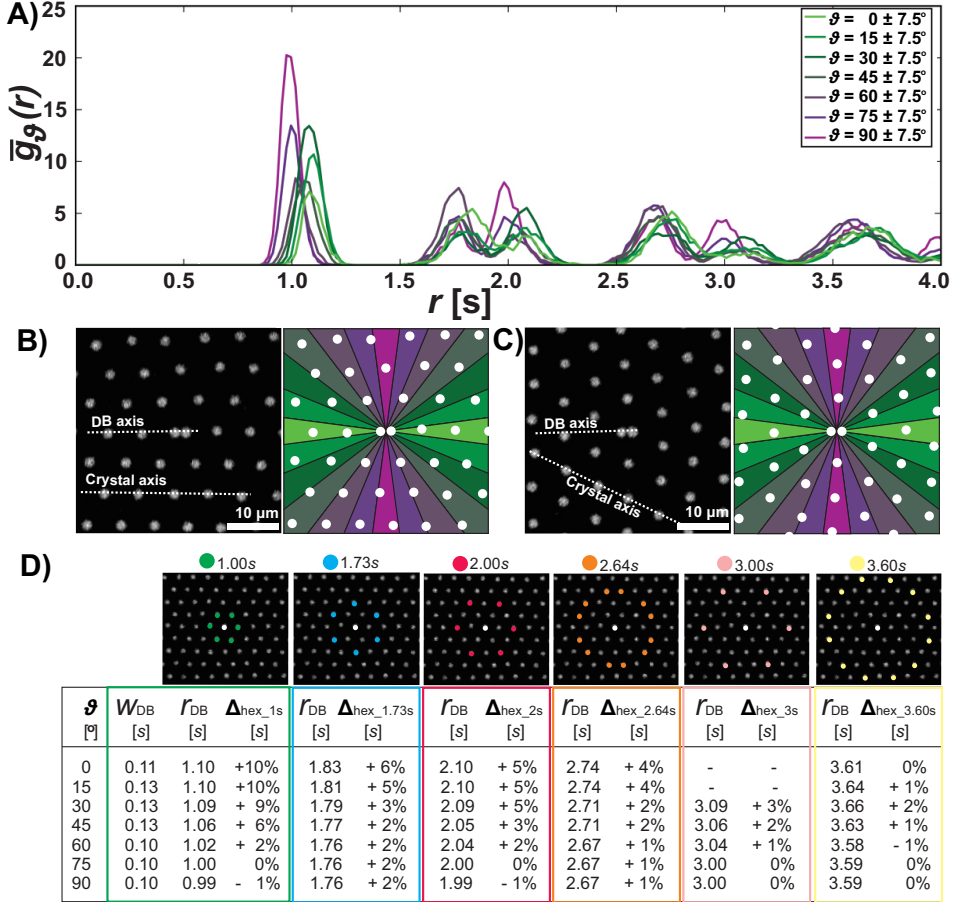
ϑ	W_{DB}	r_{DB}	Δ_{hex_1s}	r_{DB}	$\Delta_{hex\_1.73s}$	r_{DB}	Δ_{hex_2s}	r_{DB}	$\Delta_{hex\_2.64s}$	r_{DB}	Δ_{hex_3s}	r_{DB}	$\Delta_{hex\_3.60s}$
[º]	[s]	[s]	[s]	[s]	[s]	[s]	[s]	[s]	[s]	[s]	[s]	[s]	[s]
0	0.11	1.10	+10%	1.83	+ 6%	2.10	+ 5%	2.74	+ 4%	-	-	3.61	0%
15	0.13	1.10	+10%	1.81	+ 5%	2.10	+ 5%	2.74	+ 4%	-	-	3.64	+ 1%
30	0.13	1.09	+ 9%	1.79	+ 3%	2.09	+ 5%	2.71	+ 2%	3.09	+ 3%	3.66	+ 2%
45	0.13	1.06	+ 6%	1.77	+ 2%	2.05	+ 3%	2.71	+ 2%	3.06	+ 2%	3.63	+ 1%
60	0.10	1.02	+ 2%	1.76	+ 2%	2.04	+ 2%	2.67	+ 1%	3.04	+ 1%	3.58	- 1%
75	0.10	1.00	0%	1.76	+ 2%	2.00	0%	2.67	+ 1%	3.00	0%	3.59	0%
90	0.10	0.99	- 1%	1.76	+ 2%	1.99	- 1%	2.67	+ 1%	3.00	0%	3.59	0%

FIGURE 6.14: Anisotropic crystal distortion by dumbbells with six NNs. A) The averaged $g_\vartheta(r)$, $\bar{g}_\vartheta(r)$, obtained by combining all positional data of the spheres into the range $\vartheta \epsilon [0°$, $90°]$. The distance r at which a neighboring sphere is positioned decreases with increasing ϑ. ϑ is related to the dumbbell orientation β, for example the NNs position at B) $\vartheta \simeq 0°$ and $60°$ for $\beta = 0°$ and at C) $\vartheta \simeq 30°$ and $90°$ for $\beta = 30°$. D) Comparison of the observed peak positions to the expected peak positions for neighboring spheres in an hexagonal crystal, $r_{hex} = 1.00$, 1.73, 2.00, 2.64, 3.00 and 3.60s. For the NNs of the dumbbell deviations of -1 to +10% were measured compared to r_{hex}. For the next NNs deviations of -1 to +6% were found and the differences decrease further with r. Compared to $r_{hex} = 3.60s$ differences of 1 or 2% were found, indicating that the hexagonal order in the crystal had almost completely restored. Therefore, the hexagonal order was only locally anisotropically distorted and dumbbells with six NNs occupied one lattice position in the hexgonal crystal.

(Figure 6.9B).

This four-fold symmetry allowed us to combine and average the data into an effective angular range of $\vartheta \epsilon [0° , 90°]$. From this effective angular range we calculated an averaged $\bar{g}_\vartheta(r)$ (see Figure 6.14A). A relation between ϑ and r can be observed, where the distance r at which a nearest neighbor is located decreases with increasing ϑ. NNs at $\vartheta = 90°$ were positioned closer to the COM of the dumbbell compared to NNs positioned in line with the dumbbell axis at $\vartheta = 0°$, resulting in an anisotropic distortion of the hexagonal order locally around the dumbbell.

Interestingly, the first peak for all values of ϑ slightly shifts around $r = 1s$, which indicates that the dumbbell rotated in time affecting the position of the surrounding spheres in turn. The effect of β on ϑ is illustrated in Figure 6.14B and 6.14C by overlaying the position of the spheres found in confocal microscopy images with a schematic of ϑ, corresponding to the colors used in the Figure 6.14A. When the dumbbell is aligned with the crystal orientation, $\beta = 0°$, the NNs position at $\vartheta \simeq 0°$ and 60° (Figure 6.14B). For a dumbbell oriented at $\beta = 30°$ the six NNs are located at $\vartheta \simeq 30°$ and 90° (Figure 6.14C).

Voronoi tesselations indicated that dumbbells with six NNs occupied one lattice site in the hexagonal crystal (see Figure 6.7A2 and 6.7A3). To quantify the anisotropic distortion of the hexagonal crystal we therefore compared the position of the neighboring spheres to expected values for neighborings spheres in an hexagonal crystal with lattice spacing s, $r_{hex} = 1.00, 1.73, 2.00, 2.64, 3.00, 3.46$ and $3.60s$ (Figure 6.14D). The NNs around the dumbbell were positioned at $r = 0.99s$ to $1.10s$, with the shortest distance r for spheres at $\vartheta = 90°$ and the largest distance r for spheres at $\vartheta = 0°$. These distances deviate by -1 to +10% from the expected value, $r_{hex} = 1s$, for NNs in a hexagonal crystal. The full width at half maximum of the peaks w_{DB} originating from the NNs is similar for all ϑ-values, indicating that all NNs had similar freedom of motion. In the hexagonal crystal, neighboring spheres in the second ring are expected at $r_{hex} = 1.73$ and $2.00s$. The second NNs of the dumbbell located at distances r deviating by -1 to +6% from the expected values for the hexagonal crystal. The differences in the position of the neighboring spheres decreased with increasing distance r. Compared to $r_{hex} = 3.60s$ small deviations, 1 to +2%, were observed which indicates that the hexagonal order had almost completely restored. This means that dumbbells with six NNs occupy one lattice position in the crystal and distort the hexagonal order only locally.

Crystal distortion by dumbbells with seven NNs

Dumbbells with $s_{DB} = 1.27 \pm 0.14d$ were typically surrounded by seven NNs, which introduced an isolated dislocation characterized by the insertion of two
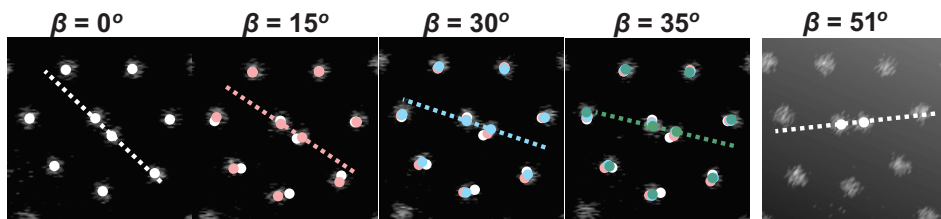
FIGURE 6.15: Confocal microscopy images of a dumbbell with seven NNs rotating in a crystal with $s = 2.67 \pm 0.17d$. At $\beta = 0°$ the dumbbell is aligned with the crystal orientation. Rotation of the dumbbell to $\beta = 15°$ resulted in the displacement of the four NNs on the line dislocation side of the dumbbell. Rotation to $\beta=30°$ and subsequently 35° induced the displacement of all particles. Although not observed at this lattice spacing, it is expected that at $\beta = 51°$ a similar situation to $\beta = 0°$ will occur, since 360/7=51°.

semi-infinite rows in the hexagonal crystal (see Figure 6.6B1). Isolated dislocations change the translational order in the long range and the orientational order locally. The dumbbell orientation was therefore determined with respect to the crystal orientation measured at sigficant distance from the dumbbell.

The introduction of two halfrows in the crystal lead to an asymmetry in the surrounding crystal between the two sides of the dumbbell axis. Confocal microscopy images of a rotating dumbbell with seven NNs at different points in time are shown in Figure 6.15. In contrast to dumbbells with six and eight NNs, the crystal orientation is not a symmetry axis for the neighboring spheres, as can be observed at $\beta = 0°$. When the dumbbell rotated to $\beta = 15°$ the NNs on the side of the dumbbell axis with the line dislocations were observed to change position. Upon further rotation to $\beta = 30°$ and 35° the other NNs also slightly changed position to adapt to the orientation of the dumbbell. At $\beta = 51°$ we expect a situation equal to $\beta = 0°$, since 360/7 = 51. Rotation to $\beta = 51°$ was not observed for this dumbbell, which points to an energy barrier at this lattice spacing, $s = 2.67 \pm 0.17d$, that restricted the rotational motion of the dumbbell.

For a dumbbell with seven NNs in a crystal with $s = 2.22 \pm 0.11d$ restrictions in both the translational and rotational motion were observed from the trajectories of the particles and the probability density plot of the position of the dumbbell $P(r)$ (Figure 6.16A). The strongly confined dumbbell oriented at -22° $< \beta <$ 22° only (see Figure 6.16B) and preferentially aligned parallel to the crystal orientation axis, $\beta = 0°$. The confinement potential of the dumbbell $U(\beta)$, calculated using $P(\beta)$, showed a confinement energy of -5 $k_B T$ at $\beta = 0°$ (Figure 6.16C). Analysis of 34 individual dumbbells with seven NNs yielded a similar result; an average β-value of 6.5 ± 4.7°.

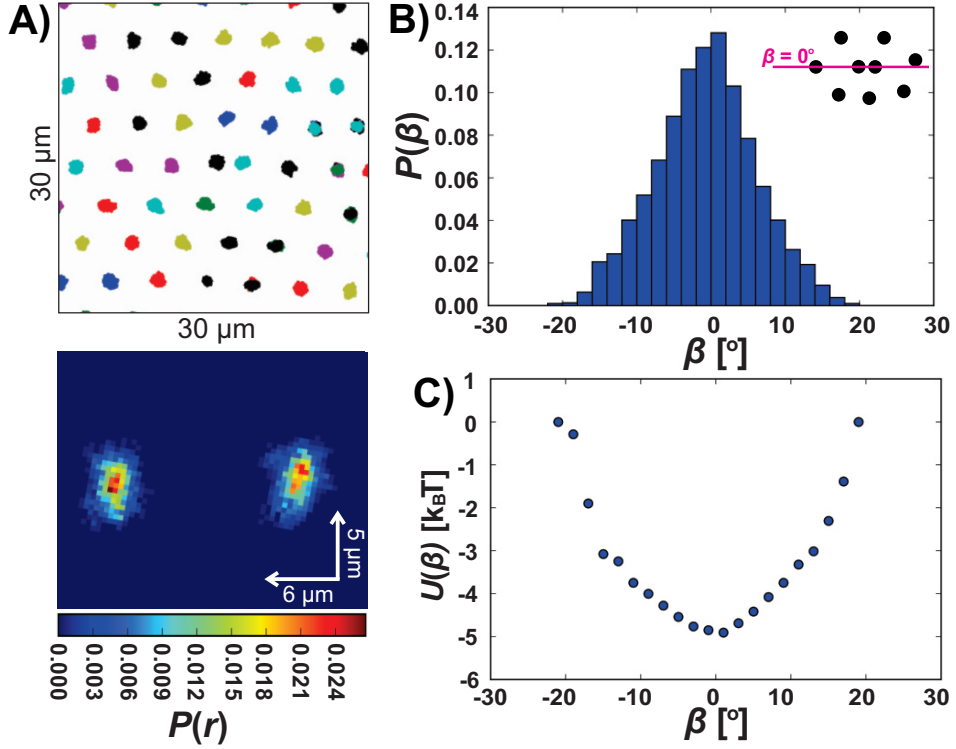To explain why dumbbells with seven NNs preferably align parallel to the crystal

FIGURE 6.16: Trajectories and preferred orientation of a dumbbell with seven NNs in a crystal with $s = 2.22 \pm 0.11d$, obtained from 3162 measurements collected in 6.4 minutes. A) The trajectories (top) of a dumbbell with seven NNs and the surrounding spheres and the probability density plot of the position of the dumbbell $P(r)$ (bottom). The dumbbell was largely confined in the crystal and the translational and rotational motion were restricted. B) $P(\beta)$, dumbbell orientations of $-22° < \beta < 22°$ were measured with the highest probabilty at $\beta = 0°$. C) The confinement potential $U(\beta)$ calculated from $P(\beta)$ shows a confinement energy of $-5k_BT$ at $\beta = 0°$.

orientation, we refer to the behavior of isolated dislocations in hexagonal crystals. An isolated dislocation directs parallel to the Burgers vector originating from the two halfrows inserted in the crystal.[190] The Burgers vector can be determined by drawing a closed circuit, a Burgers circuit, around a fixed point in a crystal. A Burgers circuit around a dumbbell with seven NNs is drawn in Figure 6.17A. By applying the same circuit to an hexagonal crystal of spheres the circuit is not closed and the Burgers vector is the vector connecting the start and finish point of the circuit (Figure 6.17B). This vector is directed parallel to the crystal orientation and always perpendicular to an isolated dislocation, as shown in the Voronoi
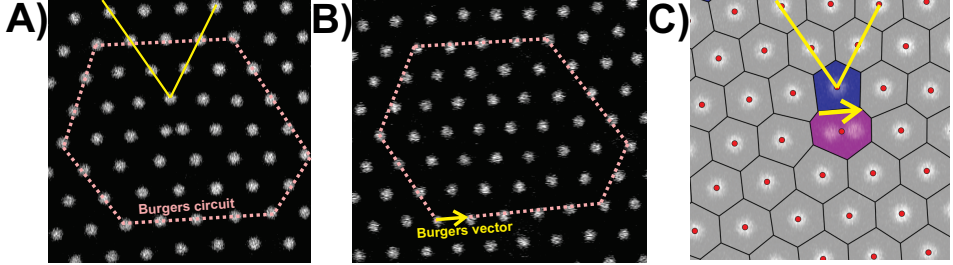
FIGURE 6.17: The Burgers circuit and Burgers vector in a hexagonal crystal with an isolated dislocation originating from a dumbbell with seven NNs. A) A closed Burgers circuit drawn (dotted line) around the dumbbell. The two inserted semi-infinite rows are indicated by the yellow lines. B) The Burgers circuit of (A) applied to a hexagonal crystal of spheres. The circuit is closed by the Burgers vector which connects the start and finish point of the Burgers circuit. The direction of the Burgers vector is equal to the crystal orientation. C) Voronoi diagram of a dumbbell with seven NNs with the Burgers vector illustrated perpendicular to the isolated dislocation.

diagram of the dumbbell in Figure 6.17C. Dumbbells with seven NNs therefore preferably orient at $\beta = 0°$.

To analyse the position of the neighboring spheres we calculated $g_\vartheta(r)$ for a dumbbell with seven NNs in a crystal with $s = 2.33 \pm 0.12d$. $g_\vartheta(r)$ was plotted separately for $\vartheta \epsilon [0°, 180°]$ and $\vartheta \epsilon [180°, 360°]$, see Figure 6.18A. On one side of the dumbbell axis, $\vartheta \epsilon [0°, 180°]$, strong peaks of NNs were observed at $\vartheta = 0, 45, 105$ and $165 \pm 7.5°$ (top graph in Figure 6.18A). Depending on the orientation of the dumbbell the nearest neighbor located at $\vartheta = 165 \pm 7.5°$ could also be found at $\vartheta = 180 \pm 7.5°$. On the other side of the dumbbell axis, $\vartheta \epsilon [180°, 360°]$, the NNs positioned at $\vartheta = 210, 270, 315$ and $360 \pm 7.5°$ (bottom graph in Figure 6.18A). The location of the NNs is illustrated in the top left of the graphs. Peaks in $g_\vartheta(r)$ of NNs positioned at other ϑ-values were small or absent, which again points to the restrictions in the rotational freedom of the dumbbell.

The full width at half maximum of the peaks in $g_\vartheta(r)$ originating from the NNs, w_{NNs}, was similar for most NNs (Figure 6.18B). w_{NNs} of the nearest neighbor at $\vartheta = 210°$ was largest which is in agreement with qualitative observations for a dumbbell rotating in time, see Figure 6.15. The NNs were located at distances $r = 0.86s$ to $1.17s$, which is a difference of 36%. The NNs at $\vartheta = 105°$ and $270°$ were positioned at $r = 0.86s$ and $0.89s$, respectively, while the NNs at $\vartheta = 0, 165, 210$ and $315 \pm 7.5°$ were found at distances r ranging from $1.11s$ to $1.17s$. Only the nearest neighbor located at $\vartheta = 45°$ was positioned at the expected lattice position for NNs in a hexagonal crystal, $r = 1.02s$. These findings explain the semi-splitted peak observed in the $g(r)$ for the NNs of a dumbbell with seven NNs shown
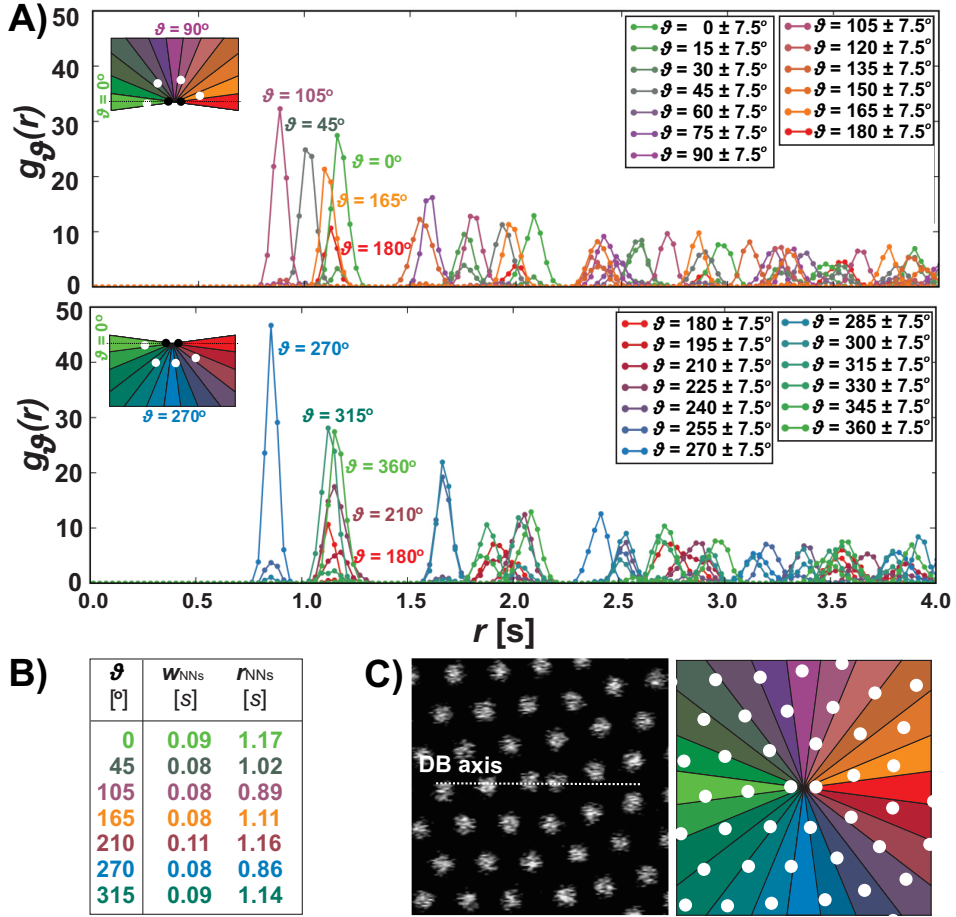
FIGURE 6.18: Positional information of spheres surrounding a typical dumbbell with seven NNs in a hexagonal crystal with $s = 2.33 \pm 0.12d$ calculated from 5440 measurements collected over three minutes. A) Restricted angular radial distribution functions $g_\vartheta(r)$ covering both sides of the dumbbell axis, $\vartheta \epsilon [0°, 180°]$ (top) and $\vartheta \epsilon [180°, 360°]$ (bottom). No symmetry is observed in the position of the surrounding spheres. B) The full width at half maximum of peaks in $g_\vartheta(r)$ originating from the NNs, w_{NNs}, is largest for the nearest neighbor positioned at $\vartheta = 210°$. The distance r at which the NNs position deviates from $r = 0.86s$ to $1.17s$. C) Confocal microscopy image of a dumbbell with seven NNs and an illustration of the ϑ-values of the spheres surrounding the dumbbell.

in Figure 6.8B. A confocal microscopy image of a dumbbell with seven NNs is shown in Figure 6.18 with the positions of the spheres overlaying an illustration
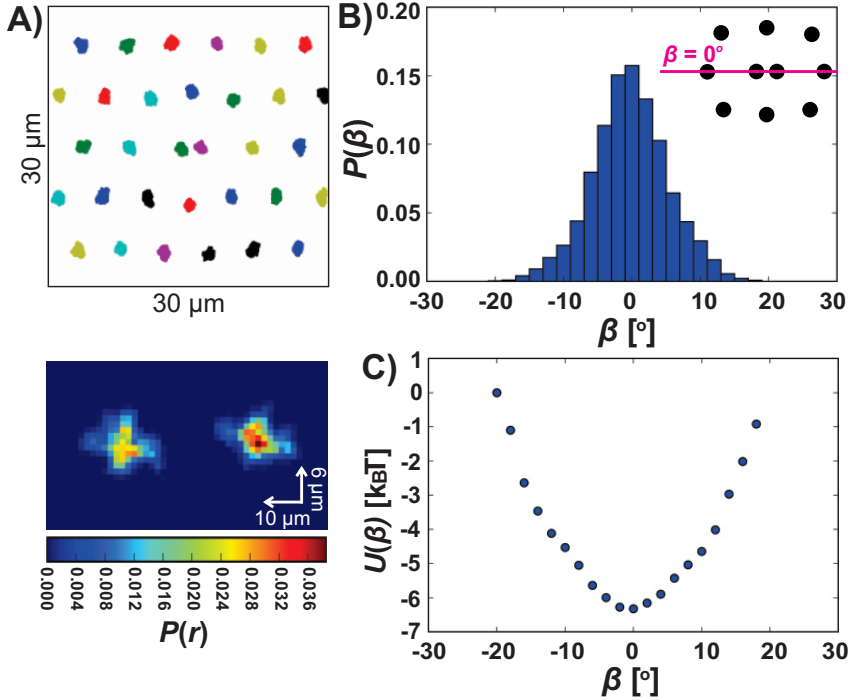
FIGURE 6.19: Trajectories and preffered orientation of a typical dumbbell with eight NNs in a crystal with $s = 3.20 \pm 0.15d$ calculated from 7090 measurments collected in two minutes. A) Trajectories of the dumbbell and the surrounding spheres (top) and the probability density plot of the position of the dumbbell $P(r)$ (bottom). Both the translational and rotational motion of the dumbbell were restricted. The limited translational motion was directed perpendicular or parallel to the crystal orientation axis, resulting in a cross-profile in $P(r)$. B) $P(\beta)$, dumbbell orientations of $-22° < \beta < 22°$ were measured where the dumbbell preferentially oriented parallel to the crystal orientation axis, at $\beta = 0°$. C) The confinement potential $U(\beta)$ calculated from $P(\beta)$ shows a strong confinement energy of -7 k_BT at $\beta = 0°$.

of the ϑ-values of the neighboring spheres to visualize the asymmetry in the crystal around a dumbbell with seven NNs.

Crystal distortion by dumbbells with eight NNs

Dumbbells with large intradumbbell distances, $s_{DB} = 1.42 \pm 0.17d$, were often surrounded by eight NNs. We analysed the orientation of a typical dumbbell with eight NNs in a crystal with $s = 3.20 \pm 0.15d$. The trajectories of the dumbbell and the surrounding spheres travelled over several minutes show that the parti-
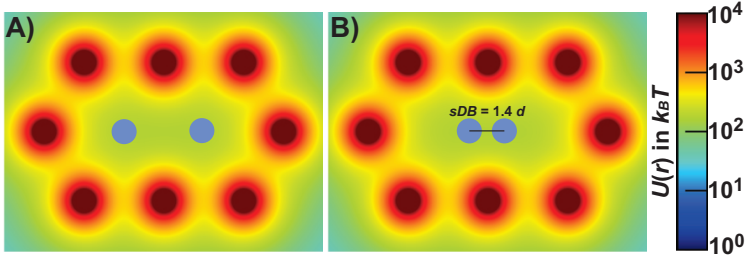
FIGURE 6.20: The potential energy landscape A) of eight neighboring spheres on two hexagonal lattice positions and B) around a dumbbell with $s_{DB} = 1.4d$ occupying two lattice sites.

cles were confined to their lattice position in the crystal (Figure 6.19A top). In the probability density plot of the position of the dumbbell, $P(r)$, the limited translational motion of the dumbbell was only directed parallel and perpendicular to the crystal orientation axis (Figure 6.19A bottom).

Analysis of the dumbbell orientation revealed that the dumbbell oriented at -22° $< \beta < 22°$, with a high probability to orient parallel to the crystal orientation, at $\beta = 0°$, see Figure 6.19B. The confinement potential calculated from $P(\beta)$ shows strong confinement of the dumbbell at $\beta = 0°$ with a confinement energy of -7 $k_B T$ (Figure 6.19C). Rotation of the dumbbell likely requires large distortions in the surrounding crystal, which is energetically unfavorable. Similar results were obtained by analysis of single confocal microscopy images of 22 different dumbbells with eight NNs, $\beta = 3.6 \pm 2.5°$.

In $g(r)$ of a dumbbell with eight NNs two separate peaks were observed around $r = 1s$, which points to large differences in the distance r at which the eight NNs are positioned (Figure 6.8). To include the anisotropy of the dumbbell in our analysis we calculated the $g_\vartheta(r)$ of a typical dumbbell with eight NNs, for $\vartheta \epsilon [0°, 90°]$, [90°, 180°], [180°, 270°] and [270°, 360°], separately (see Figure 6.21). The four $g_\vartheta(r)$ graphs show peaks at similar positions and this symmetric behavior in the position of the spheres allowed us to combine and average the positional data into an effective angular range of $\vartheta \epsilon [0°, 90°]$. In the resulting $\bar{g}_\vartheta(r)$ large differences were observed in the peak positions of the NNs (see Figure 6.22A). The peaks originating from NNs located at $\vartheta = 75°$ and 90° were completely separated from the peaks originating from NNs at $\vartheta = 0°$ to 60°. The distance r at which the NNs at $\vartheta = 45°$ and 0° were positioned differ by 29% and 45%, respectively, from the distance r where the NNs at $\vartheta = 90°$ were found. This explains the presence of the two peaks around $r = 1s$ in the $g(r)$ for a dumbbell with eight NNs (Figure 6.8). A confocal microscopy image of a dumbbell with eight NNs is shown in Figure 6.22B with an illustration of the ϑ-values of the surrounding spheres. Voronoi
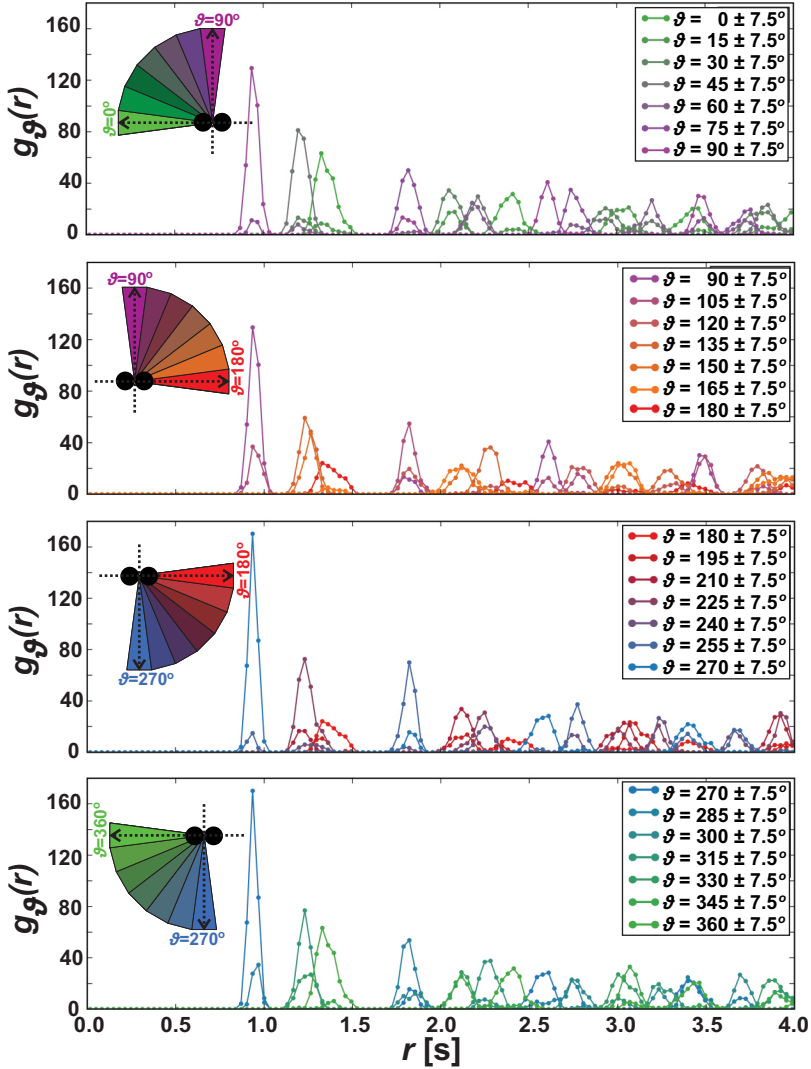
FIGURE 6.21: Restricted angular radial distribution functions $g_\vartheta(r)$ of a typical dumbbell with eight NNs in a crystal with $s = 3.20 \pm 0.15d$, obtained from 7090 measurements in two minutes. The four $g_\vartheta(r)$ graphs contain positional information of spheres surrounding the dumbbell at $\vartheta \epsilon [0°, 90°]$, $[90°, 180°]$, $[180°, 270°]$ and $[270°, 360°]$, respectively. Peaks are observed at similar distances r in the four graphs, pointing to symmetric behavior of the spheres in the four quadrants around the dumbbell.
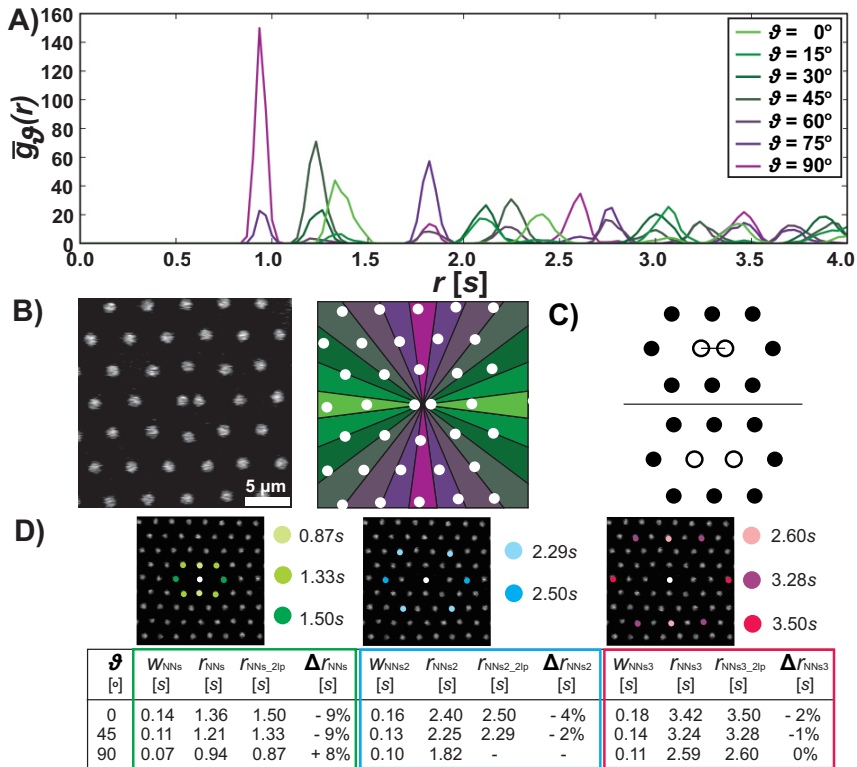
FIGURE 6.22: Crystal distortion by dumbbells with eight NNs. A) $\bar{g}_\vartheta(r)$ of a dumbbell with eight NNs with all positional data of the surrounding spheres projected to $\vartheta \epsilon [0°, 90°]$. The distance r at which the spheres positioned largely depended on ϑ and the NNs were predominantly located at $\vartheta = 0°$, $45°$ and $90°$. B) Confocal microscopy image of a dumbbell oriented at $\beta = 0°$ with an illustration of the ϑ-values of the surrounding spheres. C) Illustration of an hexagonal crystal where the dumbbell occupies two lattice positions. D) Comparison of the positions of spheres around the dumbbell to the positions expected around a sphere occupying two lattice sites in a hexagonal crystal. The positions of the NNs around the dumbbell differed by -9 to +8% from the expected positions, $r = 0.87s$, $1.33s$ and $1.50s$. In the second row of neighboring spheres, NNs2, deviations of -2 to -4% were found. In the third ring of neighboring spheres, NNs3, deviations of -1 and -2 % were measured, indicating that the hexagonal order has almost completely restored at this distance. Dumbbells with eight NNs occupy two lattice sites in the hexagonal crystal and distort the order only locally. The full width half maximum of the peaks originating from the neighboring spheres around the dumbbell, w_{NNs}, w_{NNs2} and w_{NNs3}, decreased with increasing ϑ.

114

diagrams indicated that dumbbells with eight NNs occupied two lattice sites in a hexagonal crystal (Figure 6.7C2, 6.7C3 and 6.22C). We therefore compared the positions of the neighboring spheres with the expected lattice positions of the neighbors of a sphere occupying two lattice sites (Figure 6.22D). Since in $\bar{g}_\vartheta(r)$ the peaks at $\vartheta = 0°$, $45°$ and $90°$ were most pronounced, we only compared the positions of neighboring spheres at these ϑ-values. The full width half maximum of the peaks originating from the neighboring spheres around the dumbbell, w_{NNs}, w_{NNs2} and w_{NNs3}, decreased with increasing ϑ. This indicates that the confinement of the surrounding spheres decreased with increasing ϑ. For the NNs differences of -9 to +8% in the distance r at which the spheres were located were observed compared to the values expected. The deviations quickly decreased with increasing distance r. In the third row of NNs, NNs3, differences of only -1 and -2% were measured compared to the expected values which indicated that the hexagonal order had almost completely restored. Dumbbells with eight NNs evidently occupied two lattice sites in the hexagonal crystal and distort the crystal only locally.

6.4   Further Discussion

We showed that dumbbells with s_{DB}-values close to the diameter of the particles were surrounded by six NNs and that the number of NNs increased to seven and eight with the intradumbbell distance s_{DB}. All dumbbells distorted the hexagonal order of the surrounding spheres, either locally or over long distances. The preferred orientation of the dumbbells with respect to the crystal orientation depended on the number of NNs and the lattice spacing s. At short lattice spacings dumbbells with six NNs favored $\beta = 30°$, whereas dumbbells with seven or eight NNs preferentially oriented at $\beta = 0°$. The energy cost for the dumbbell to rotate in the crystal increased with s_{DB} and with increasing confinement. Dumbbells with six NNs have relatively more rotational freedom compared to dumbbells with seven or eight NNs at similar lattice spacings. The surroundings of dumbbells with six NNs are highly symmetric, while an strongly anisotropic environment was observed for dumbbells with seven and eight NNs. The energy cost for rotation is therefore larger for dumbbells with seven and eight NNs compared to dumbbells with six NNs.

Since dumbbells distort the hexagonal order is it likely that pairs of dumbbells interact at short distances. In Figure 6.23A-C confocal microscopy images are shown of dumbbells as NNs. Two dumbbells with short s_{DB} aligned parallel, were observed to occupy two lattice sites in the crystal (Figure 6.23A). Three lattice sites were occupied by two dumbbells aligned parallel, but in sequence (Figure 6.23B). Dumbbells could also align perpedicular as illustrated in Figure 6.23C. The preferred situation probably depends on the lattice spacing s and s_{DB} of
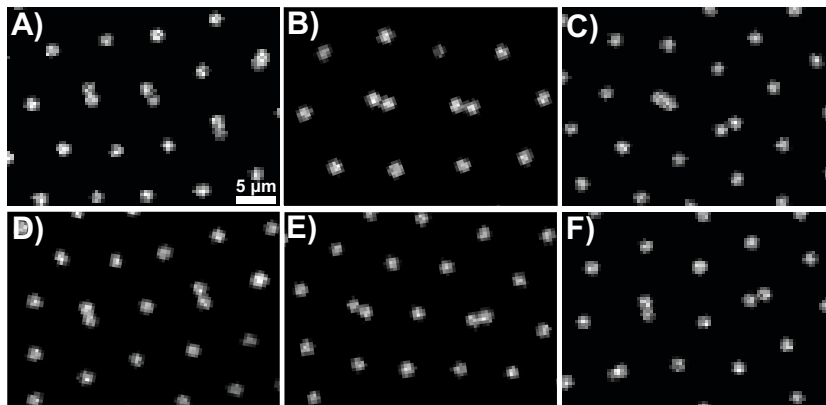
FIGURE 6.23: Orientations of neighboring dumbbells (A-C) and dumbbells separated by one crystal row (D-F). The dumbbells oriented parallel or perpendicular. Two neighboring dumbbells could occupy two (A) or three (B) lattice positions in the hexagonal crystal depending on their orientation with respect to each other and s_{DB}.

the dumbbells. Similar orientations were also observed for dumbbells separated by one crystal row of particles, Figure 6.23D-F. Further research on neighboring dumbbells should provide information on the interaction between dumbbells and their effect on the hexagonal order in the crystal. Investigation of the effect of other anisotropic impurities such as chains, triangular and square shapes (Figure 6.5) on the hexagonal order could also provide additional information.

6.5 Conclusions

We studied how repulsive pMMA spheres and anisotropic impurities arranged at a flat fluid interface between a glycerol:water (85:15) and CHB:cis-decalin (70:30) phase. Spheres ordered on a hexagonal lattice where their motion was restricted to one lattice site at short lattice spacings. At the fluid interface three types of impurities were observed in the crystal: (1) spherical objects significantly smaller or larger with respect to the particle diameter, (2) colloid stabilized droplets of the aqueous phase in the organic phase and (3) anisotropic clusters of spheres. Analysis of anisotropic clusters formed by two spheres, dumbbells, showed that the distance between the two spheres, the intradumbbell distance s_{DB}, differed per dumbbell. As s_{DB} increased the number of nearest neighbors also increased from six to a maximum of eight. We speculated that the formation of the anisotropic clusters originated from small aqueous droplets between the spheres forming the dumbbell.

The orientation of the dumbbells with respect to the hexagonal crystal depended on s_{DB} and the lattice spacing. At short lattice spacings the rotational and translation motion of the dumbbells was restricted and a preferred orientation of the dumbbell axis with respect to the crystal orientation was found. Dumbbells with six nearest neighbors preferably oriented at $30°$ with respect to the crystal direction and occupied one lattice site in the hexagonal crystal. The position of the surrounding spheres depended on the dumbbell orientation and the hexagonal order was locally anisotropically distorted. Dumbbells with seven nearest neighbors distorted the translational order in the crystal over long ranges by the introduction of an isolation dislocation and preferably oriented parallel to the crystal orientation. At larger s_{DB} dumbbells were surrounded by eight nearest neighbors occupying two lattice sites in the hexagonal crystal. The rotational motion of these dumbbells was strongly restricted and the dumbbells preferentially oriented in line with the crystal orientation. The confinement potential of the dumbbells and the surrounding spheres showed confinement energies up to -7 $k_B T$. The anisotropic energy landscape around the dumbbells originated from the repulsion between the two spheres forming the dumbbell and the surrounding spheres in the crystal.

Our results emphasize that the distortion of anisotropic impurities differ from isotropic impurities, which will likely also affect the physical properties of colloidal crystals. We therefore encourage future studies on the affect of anisotropic impurities on crystals.